

Strong tunable phonon-phonon interactions induced by silicon-vacancy centers in one-dimensional chiral phononic waveguides

Cai-Peng Shen, Xing-Liang Dong, Jia-Qiang Chen, Xin-Lei Hei, Yi-Fan Qiao, Bo-Long Wang, and Peng-Bo Li^{*}

Ministry of Education Key Laboratory for Nonequilibrium Synthesis and Modulation of Condensed Matter, Shaanxi Province Key Laboratory of Quantum Information and Quantum Optoelectronic Devices, School of Physics, Xi'an Jiaotong University, Xi'an 710049, China

 (Received 16 March 2022; revised 24 June 2022; accepted 16 August 2022; published 30 August 2022)

In solid quantum systems, strong phonon-phonon repulsive or attractive interactions are difficult to achieve. The highly adjustable phonon-phonon interactions created by silicon-vacancy (SiV) centers in a one-dimensional chiral phononic waveguide are investigated in this paper. Under specific situations, phonon-phonon attractive or repulsive interactions between the chiral transport phonons are created when they are scattered by two-level or three-level structural SiV centers. Furthermore, by modulating the laser Rabi frequencies and detunings, the resultant attractive or repulsive interactions between phonons can be adjusted over a large frequency range. Single-phonon creation and phonon manipulation in solid acoustic quantum information processing could benefit from the tunable phonon-phonon interactions.

DOI: [10.1103/PhysRevA.106.023717](https://doi.org/10.1103/PhysRevA.106.023717)

I. INTRODUCTION

Solid-state quantum systems, such as superconducting circuits [1–3], mechanical oscillators [4–8], magnons [9–14], and diamond color centers [5,15–21], have attracted extensive attention in quantum science and technology. Different solid-state quantum systems have been exploited to constitute quantum hybrid systems [22–24] to perform various quantum information processing operations for the complementary advantages. For example, spin squeezing states have been generated using diamond nitrogen-vacancy centers coupled with clamped mechanical resonators [25] and silicon-vacancy (SiV) centers coupled with acoustic waveguides [26]. Topological phases are simulated using the SiV-center-waveguide system [27,28]. The magnon-photon-phonon entanglement [29] and squeezed states of magnons and phonons [30] have also been explored in cavity magnomechanical systems. Phonons play a crucial role in interfacing the various physical solid systems in these quantum information processing techniques.

In solid quantum systems, phonons can couple with magnons via the magnetostrictive interactions [29] and interact with SiV centers through strain coupling [31,32], and also couple with superconducting qubits through mechanical as well as electromagnetic processes [33]. Thus the phonons are useful to integrate diverse solid quantum systems in quantum information processing. Recently, much attention has been paid to the manipulations of phonons, such as phonon blockade [34–39] and phonon nonreciprocal transport [40–48]. Since phonons are charge neutral and spinless, strong phonon-phonon interactions at a few-phonon level are difficult to realize. To accomplish effective phonon-phonon interactions, strong nonlinearity or nonlin-

ear response by phonon-matter coupling is necessary. For instance, phonon blockade has been studied using large quadratic optomechanical coupling [37,49] or strong coupling in spin-mechanical systems [38,50]. In Ref. [51] the attractive (bunching) phonon-phonon interactions, induced by strong phonon-spin strain coupling, were examined in one-dimensional phononic waveguide, whereas the realization of repulsive (antibunching) interactions requires a significant energy difference between the incident two phonons and the interactions cannot be adjustable. These constraints may cause the linear dispersion approximation to fail and they are not flexible enough for practical use. Thus, in solid-state acoustic quantum information processing, how to realize the more practical strongly repulsive phonon-phonon interactions is of tremendous importance.

In this work the tunable strongly correlated phonons induced by SiV centers in one-dimensional (1D) chiral phononic waveguides are studied. The phonon transport in 1D chiral phononic waveguides is directional and immune to backscattering [52–54], implying that the induced phonon-phonon interactions are unaffected by the SiV center positions. Varied numbers of two-level SiV centers (2LSCs) create different phonon correlations in the resonance situation, according to investigations. That is, the two chiral transport individual phonons become correlated bunching after being scattered by an odd number of 2LSCs, whereas the output phonons are uncorrelated after being scattered by an even number of 2LSCs. Phonon antibunching can be produced by large phononic dissipations from 2LSCs to nonguided modes. The phononic dissipations to the external environment in solid systems, on the other hand, are so modest that they are frequently ignored. It is further demonstrated that when 2LSCs are substituted by three-level SiV centers (3LSCs), phonon antibunching can occur. The scattered phonons perform stronger antibunching as the number of 3LSCs increases. Both phonon bunching and antibunching are

^{*}lipengbo@mail.xjtu.edu.cn

created under the control of laser Rabi frequency and detuning, implying that phonon-phonon interactions are adjustable, i.e., obtaining attractive or repulsive phononic interactions can be controlled by laser parameters. It also demonstrates that phonon-phonon interactions can be tuned over a broad range of phonon frequencies. The energy of the chiral transport phonons is adjusted to the same value here, making the linear dispersion assumption more acceptable and experimental implementations more viable. Tunable strong phonon-phonon correlations could aid in the generation of single phonons and expand the scope of phononic manipulation research in solid quantum science and technology.

II. MODEL

Consider N SiV centers coupled with chiral transport phonons in a 1D phononic waveguide. The 1D chiral phononic waveguide can be created from the robust unidirectional transport acoustic edge modes along the edge of a 2D phononic crystal by breaking the time-reversal symmetry [53,55] or in topological insulators with certain geometrical approaches [52,54,56]. In Ref. [53] the 1D chiral acoustic waveguide in the snowflake optomechanical crystal is utilized to transfer quantum states between separated SiV centers embedded in optomechanical cavities along the edge of optomechanical crystal. Inspired by that work, in Fig. 1(a) we study the phonon-phonon interactions induced by SiV centers in the optomechanical crystal with topological chiral transport acoustic edge modes, i.e., the 1D chiral phononic waveguide.

SiV centers are diamond defect centers with two carbon atoms replaced by one silicon atom. SiV centers possess narrow inhomogeneous broadening, strong zero-phonon line emission, and high strain susceptibility [57–63], which allows them to act as suitable qubits in solid quantum systems. Due to the spin-orbit coupling, the ground state (GS) and excited state (ES) in a SiV center would be divided into two ground sublevels and two excited sublevels, respectively. In one SiV center, there are four optical transition channels between the excited and ground sublevels, denoted by the letters A, B, C, and D in Fig. 1(b). The transition between the ground sublevels in SiV centers can be induced by strain coupling with phonons in solid acoustic systems. In this work we treat the SiV center as a three-level system with two GS sublevels $|g\rangle$ and $|f\rangle$ and one ES sublevel $|e\rangle$. Chiral transport phonons drive $|g\rangle \leftrightarrow |f\rangle$, while an external laser couples $|e\rangle \leftrightarrow |f\rangle$ with Rabi frequency Ω and energy ω_0 . The Hamiltonian of the interacting system is

$$\hat{H} = \sum_k \omega_k \hat{b}_k^\dagger \hat{b}_k + \sum_j \left(\Omega \hat{\sigma}_{ef}^j e^{-i\omega_0 t} + g_k \sum_k \hat{\sigma}_{fg}^j \hat{b}_k + \text{H.c.} \right) + \sum_j \left[\left(\omega_f - \frac{i\gamma_1}{2} \right) \hat{\sigma}_{ff}^j + \left(\omega_e - \frac{i\gamma_2}{2} \right) \hat{\sigma}_{ee}^j \right], \quad (1)$$

where the linear dispersion is assumed as $\omega_k = v_g k$ and v_g is the velocity of chiral transport phonons. In addition, \hat{b}^\dagger (\hat{b}) is the creation (annihilation) operator of phonons, ω_f (ω_e) is the energy of $|f\rangle$ ($|e\rangle$), and $\hat{\sigma}_{\mu\nu}^j$ denotes the transition operator $|\mu\rangle\langle\nu|$ of the j th SiV center. We set $\hbar = 1$ and the direction of

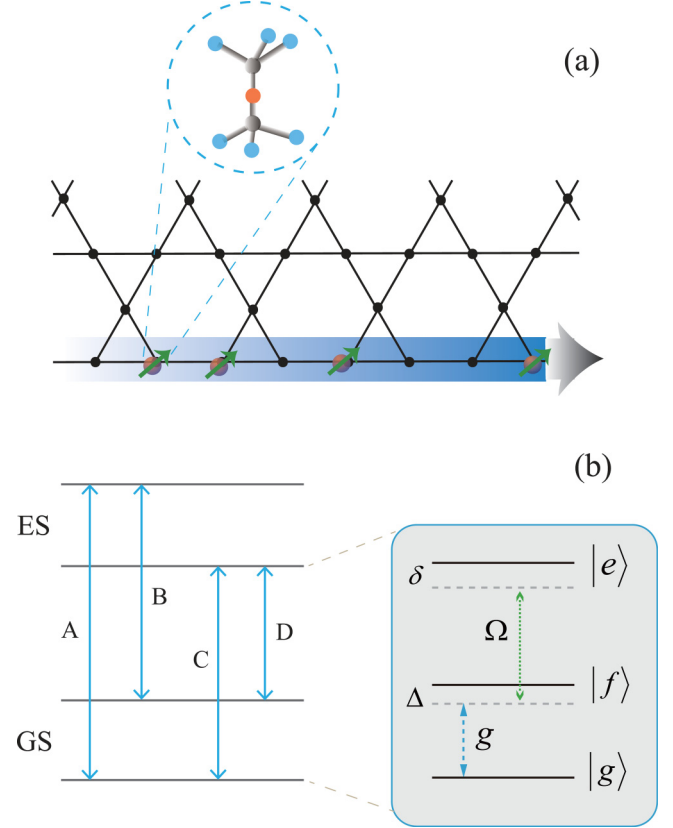


FIG. 1. (a) Topological chiral transport edge modes along the edges of 2D optomechanical crystals with snowflake shapes form a 1D chiral acoustic waveguide. SiV centers are implanted in the optomechanical cavities along the waveguide. (b) Due to spin-orbit coupling, the ground state (GS) and excited state (ES) in a SiV center would split into two sublevels, respectively. A, B, C, and D denote four optical transition channels. A three-level system is composed of two GS sublevels and one ES sublevel, denoted by $|g\rangle$, $|f\rangle$, and $|e\rangle$. The chiral transport phonons couple to the transition $|g\rangle \leftrightarrow |f\rangle$ with strength g and detuning Δ . The Rabi frequency of the optical transition $|f\rangle \leftrightarrow |e\rangle$ is Ω and δ is the phonon-optical detuning.

transmitting phonons is from left to right. Here g_k is the coupling strength between different phonon modes and ground sublevels of a SiV center, assuming $g_k \equiv g$ hereafter (Markov approximation) [64]. Further, γ_1 is the acoustic dissipation from $|f\rangle$ to nonguided modes, while γ_2 is the electromagnetic dissipation from $|e\rangle$ to the external environment. As will be mentioned below, the acoustic dissipation from $|f\rangle$ into the waveguide (guided modes) is Γ , which also characterizes the coupling strength of phonon-phonon interactions.

Adopting Fourier transforms [64–70], the Hamiltonian of the interacting system can be rewritten in real space as

$$\hat{\mathcal{H}} = -i \int dx \hat{b}^\dagger(x) \partial_x \hat{b}(x) + \sum_j \left(\Omega \hat{\sigma}_{ef}^j + \text{H.c.} \right) + \sum_j \left[\left(\omega_f - \frac{i\gamma_1}{2} \right) \hat{\sigma}_{ff}^j + \left(\omega_e - \omega_0 - \frac{i\gamma_2}{2} \right) \hat{\sigma}_{ee}^j \right] + \sum_j \left(\int dx V \delta(x - r_j) \hat{\sigma}_{fg}^j \hat{b}(x) + \text{H.c.} \right), \quad (2)$$

where $V = \sqrt{2\pi}g$ and the velocity of chiral transport phonons is set to $v_g = 1$. The acoustic spontaneous radiation from a SiV center into the guided mode can be given as $\Gamma = 2V^2$. For the transport phonons with identical energy ω , the single-phonon detuning is $\Delta = \omega_f - \omega$, while the phonon-optical detuning is $\delta = \omega_e - (\omega_0 + \omega)$, which is marked in Fig. 1(b). For weak coherent chiral transport phonons along the waveguide, we mainly focus on the correlations of two phonons mediated by the embedded SiV centers. The chiral transport of two phonons scattered by N embedded SiV centers in the waveguide can be viewed as a cascaded quantum system [71], i.e., the phonons passing through the j th SiV center can be thought of as the input state for the $(j + 1)$ th SiV center. Thus, the two-phonon correlated state would be solved after passing through the N SiV centers with this recurrent single-emitter scattering process.

III. STRONGLY CORRELATED TWO PHONONS INDUCED BY 2LSCS

In this section we focus on the chiral transport phonon correlations induced by 2LSCs. The Hamiltonian for the single 2LSC system reads

$$\hat{\mathcal{H}}_2 = -i \int dx \hat{b}^\dagger(x) \partial_x \hat{b}(x) + \left(\omega_f - \frac{i\gamma_1}{2} \right) \hat{\sigma}_{ff} + \left(\int dx V \delta(x) \hat{\sigma}_{fg} \hat{b}(x) + \text{H.c.} \right). \quad (3)$$

Accordingly, the eigenstate of $\hat{\mathcal{H}}_2$ has the form

$$|\phi\rangle = \left(\int dx_1 dx_2 \frac{1}{\sqrt{2}} \varphi(x_1, x_2) \hat{b}^\dagger(x_1) \hat{b}^\dagger(x_2) + \int dx f(x) \hat{b}^\dagger(x) \hat{\sigma}_{fg} \right) |0, g\rangle, \quad (4)$$

where E is the eigenenergy, $\varphi(x_1, x_2)$ is the two-phonon wave function, and $f(x)$ is the wave function of one phonon with the SiV center excited. Here the position of the SiV center is set to $r_1 = 0$. Substituting $|\phi\rangle$ into the eigenequation $\hat{\mathcal{H}}_2|\phi\rangle = E|\phi\rangle$, one has

$$\begin{aligned} & (-i\partial_{x_1} - i\partial_{x_2} - E)\varphi(x_1, x_2) \\ & + \frac{V}{\sqrt{2}}[\delta(x_1)f(x_2) + \delta(x_2)f(x_1)] = 0, \\ & \left(-i\partial_x + \omega_f - \frac{i\gamma_1}{2} - E \right) f(x) \\ & + \frac{V}{\sqrt{2}}[\varphi(0, x) + \varphi(x, 0)] = 0, \end{aligned} \quad (5)$$

where $\varphi(0, x) = \varphi(x, 0) = 1/2[\varphi(0^-, x) + \varphi(x, 0^+)]$. From Eq. (5), boundary relations for $x_1 < x_2$ (boson symmetry) satisfy

$$\begin{aligned} i[\varphi(x_1, 0^-) - \varphi(x_1, 0^+)] + \frac{Vf(x_1)}{\sqrt{2}} &= 0, \\ i[\varphi(0^-, x_2) - \varphi(0^+, x_2)] + \frac{Vf(x_2)}{\sqrt{2}} &= 0. \end{aligned} \quad (6)$$

Here $f(0^+) = f(0^-)$. From Eq. (5) one has $\varphi(x_1, x_2) = e^{iEr_c}G(r)$ when $x_1, x_2 \neq 0$, where $r_c = (x_1 + x_2)/2$ and $r = x_1 - x_2$. Since e^{iEr_c} is just a phase in $\varphi(x_1, x_2)$, the detailed distribution of the two phonons in the waveguide is mainly reflected by $G(r)$. Here $E = 2\omega$ is the two-phonon total energy. According to the different space distributions of phonons, $G(r)$ can be represented as [71]

$$G(r) = \begin{cases} G_{\text{in}}(r), & x_1 < x_2 < 0 \\ G_0(r), & x_1 < 0 < x_2 \\ G_{\text{out}}(r), & 0 < x_1 < x_2, \end{cases} \quad (7)$$

where $G_{\text{in}}(r)$ denotes the input two-phonon amplitude before interacting with the SiV center, $G_0(r)$ represents the amplitude of one phonon that passes through the SiV center but not the other, and $G_{\text{out}}(r)$ describes the amplitude of the output two-phonons after crossing the emitter. Based on Eqs. (5)–(7), for a given input two-phonon wave function, the output two-phonon wave function after passing through the SiV center can be solved. As for N embedded SiV centers, the input phonon wave function for the $(j + 1)$ th SiV center is just the outgoing two-phonon wave function through the j th SiV center. Thus, the output two-phonon wave function after crossing N SiV centers could be solved by this recursion relation. The second correlation function $g_2(r)$ can be obtained based on the output phonon wave function to describe the phonon-phonon interactions, and the detailed solution will be shown in the next section.

In Fig. 2(a) the second-order correlation functions of the two chiral transport phonons are plotted after being scattered by 5, 10, and 15 SiV centers. The dissipation rate γ_1 is set to zero and the single-phonon detuning is $\Delta = 0.3\Gamma$. The equal-time second-order correlation function $g_2(0) > 1$ means that the two-phonon bunching state is induced following the scattering of chiral transport phonons by the implanted SiV centers. In Fig. 2(b), $g_2(0)$ versus single-phonon detuning is plotted for $N = 5, 10, 15$, which is larger than unity except for $\Delta = 0$ and $N = 10$. When $\Delta = 0$, different phonon correlated features arise in the cases of $N = 5, 15$ and $N = 10$, i.e., the former numbers of SiV centers would induce an obvious two-phonon bunching state, while the latter would be incapable of inducing efficient phonon-phonon interactions.

To show the correlated two-phonon features more clearly, Fig. 3 depicts the graph of $g_2(0)$ as a function of various N and Δ . As can be seen, having an odd or even numbers of SiV centers produces interesting values of $g_2(0)$ when $\Delta \simeq 0$. For the resonant case, the odd number N is associated with two-phonon bunching states [$g_2(0) > 1$] and the even number N corresponds to invalid two-phonon interactions [$g_2(0) = 1$], which is an expansion of what we discussed in Fig. 2(b). When N decreases, this effect broadens in the near-resonance range ($\Delta \approx 0$). As for N and Δ in other ranges, $g_2(0) > 1$ persist.

The scattering matrix (S matrix), which stores the scattering features and transforms incoming phonon states into output phonon states ($|\text{out}\rangle = \hat{S}|\text{in}\rangle$) [67], provides insight into the physical process behind two-phonon interactions.

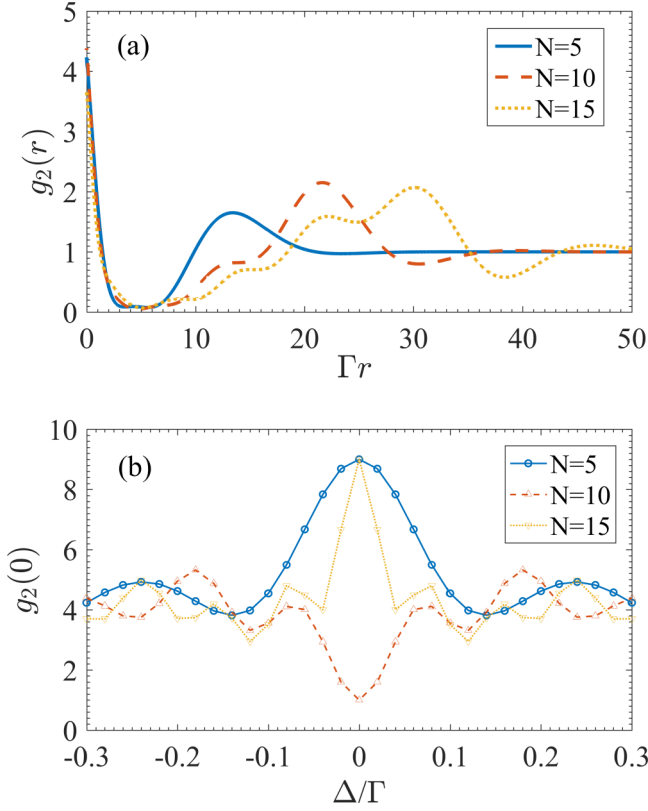


FIG. 2. (a) Plots of the two-phonon second-correlation function $g_2(r)$ after crossing various numbers of 2LSCs $N = 5, 10, 15$. The single-phonon detuning is set to $\Delta = 0.3\Gamma$. (b) Equal-time second-correlation function $g_2(0)$ versus various Δ are shown, where also $N = 5, 10, 15$. Here Γ is the phonon dissipation from a SiV center into the waveguide. Phonon dissipation to nonguided modes is set to $\gamma_1 = 0$.

The S matrix about incident phonons interacting with a 2LSC has two sorts of two-phonon eigenstates. One is a two-phonon bound state $|E\rangle_B$, whereas the other is a delocalized state $|E\rangle_D$. The eigenstates fulfill $\hat{S}|E\rangle_{D,B} = \lambda_{D,B}|E\rangle_{D,B}$, with eigenvalues $\lambda_{D,B}$. After crossing N 2LSCs, decomposing

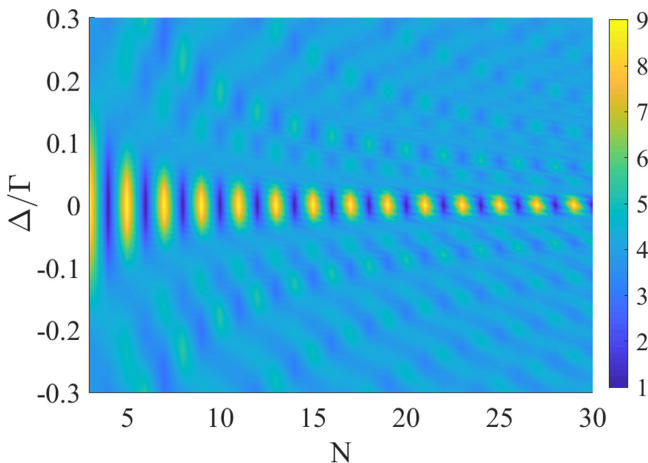


FIG. 3. Plot of $g_2(0)$ versus the single-phonon detuning Δ and the numbers of SiV centers N .

the incident state into S -matrix eigenstates produces the output two-phonon state $|\text{out}\rangle = [\int d\nu \lambda_D(\nu)^N |E\rangle_D |E\rangle + \lambda_B^N |E\rangle_B |E\rangle] |\text{in}\rangle$ [72], where ν is the frequency difference between the two phonons, $\lambda_D = \lambda_d(\Delta + \nu)\lambda_d(\Delta - \nu)$, $\lambda_d(\Delta \pm \nu) = [-(\Delta \pm \nu) - i\Gamma/2]/[-(\Delta \pm \nu) + i\Gamma/2]$, and $\lambda_B = (-2\Delta - 2i\Gamma)/(-2\Delta + 2i\Gamma)$. For different N , the distinct proportions of the two eigenstates ($\lambda_{D,B}^N$) will result in different correlations. In Fig. 4 the output two-phonon state $|\varphi_{\text{out}}\rangle$ (blue dashed line and shaded area) is decomposed into two types of eigenstates for $N = 5$ [Fig. 4(a)], $N = 10$ [Fig. 4(b)], and $N = 15$ [Fig. 4(c)]. It demonstrates that when $r = 0$, the output two-phonon state has the maximum absolute value and is mostly determined by the bound eigenstate (red dotted line). The delocalized state (green solid line) contributes little to $|\varphi_{\text{out}}\rangle$. The shape of $|\varphi_{\text{out}}(r)\rangle$ is similar to the second-order correlation function in Fig. 2(a) and it can also yield $g_2(r)$ after being normalized.

When $\Delta = 0$, one has $\lambda_D \equiv 1$ and $\lambda_B \equiv -1$. In this situation, for even numbers N , the N th powers of the two eigenvalues are both 1, and the output two-phonon state is identical to the incident two-phonon state, indicating that the two-phonon interaction is invalid. In contrast, for odd numbers N , the N th power of the delocalized eigenvalue is 1 while the N th power of the bound eigenvalue is -1 . For the nontrivial contribution from the bound eigenstate, the two-phonon interaction becomes valid. When $\Delta = 0$, $g_2(0) \equiv 1$ for even numbers N and equals a constant value (greater than 1) for odd numbers N , as shown in Figs. 2(b) and 3. The absolute values of the eigenvalues are no longer exactly unity when $\Delta \neq 0$. However, for small $|\Delta|$, $|\lambda_D| \approx 1$ and $|\lambda_B| \approx -1$ are still available. When N is small, the results mentioned above are roughly correct. The absolute values of the N th power of eigenvalues diverge significantly from unity for higher N , rendering the conclusions stated above incorrect.

The correlated two-phonon bunching states were investigated in the preceding discussion, while the nonclassical quantum antibunching states were not induced. In Fig. 5 we introduce the dissipation rate γ_1 to investigate the effect of γ_1 on $g_2(0)$, where the number of 2LSCs is $N = 3, 4, 5$. Detuning is set to zero. The result shows that as γ_1 increases in a limited range, $g_2(0)$ decreases from a value greater than unity to a value less than unity. When the expanding γ_1 reaches a critical point, $g_2(0)$ begins to rise and approach unity. That is, the phonon dissipation can induce antibunching states. On the other hand, dissipation to nonguided modes would reduce system coherence. As a result of this competition aspect, there is a critical point at which the scattered phonons best fulfill their antibunching capabilities. In contrast to electromagnetic radiation, the phonon dissipation to nonguided modes in solid systems is so small that it is usually ignored. In practice, phonon antibunching states can be difficult to create with substantial dissipation. In the following section we look at the issue of inducing phonon antibunching states.

IV. STRONGLY TUNABLE TWO-PHONON CORRELATIONS INDUCED BY 3LSCS

The chiral transport phonons scattered by 3LSCs are the topic of this section, where a laser is applied to couple

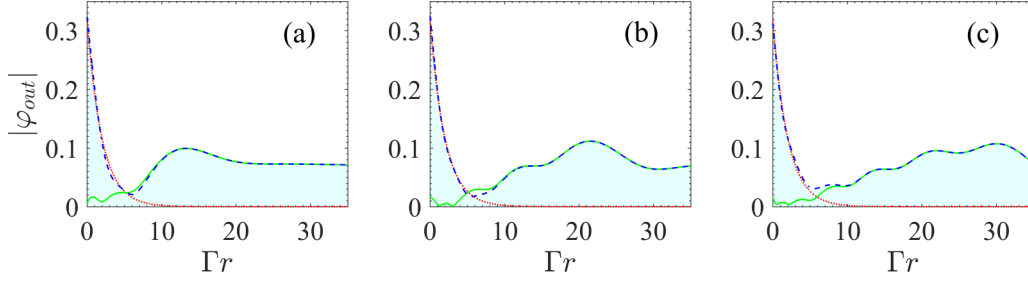


FIG. 4. Absolute value of the output two-phonon wave function $|\varphi_{\text{out}}(r)|$ (blue dashed line and shaded area) after being scattered by (a) 5, (b) 10, and (c) 15 2LSCs. Here $|\varphi_{\text{out}}(r)|$ is decomposed into two types of scattering eigenstates. One is a bound state (red dotted line), while the other is a delocalized state (green solid line). The parameters are the same as those in Fig. 2(a).

$|e\rangle \leftrightarrow |f\rangle$ in SiV centers. The Hamiltonian for a single 3LSC coupling with phonons is expressed as

$$\begin{aligned} \hat{H}_3 = & -i \int dx \hat{b}^\dagger(x) \partial_x \hat{b}(x) + (\Omega \hat{\sigma}_{ef} + \text{H.c.}) \\ & + \left(\int dx V \delta(x) \hat{\sigma}_{fg} \hat{b}(x) + \text{H.c.} \right) \\ & + \omega_f \hat{\sigma}_{ff} + \left(\omega_e - \omega_0 - \frac{i\gamma_2}{2} \right) \hat{\sigma}_{ee}. \end{aligned} \quad (8)$$

Here the phononic dissipation rate is set as $\gamma_1 = 0$. Similarly to Eq. (4), the eigenstate of Hamiltonian \hat{H}_3 has the form

$$\begin{aligned} |\psi\rangle = & \int dx_1 dx_2 \frac{1}{\sqrt{2}} \varphi(x_1, x_2) \hat{b}^\dagger(x_1) \hat{b}^\dagger(x_2) |0, g\rangle \\ & + \int dx \hat{b}^\dagger(x) [f(x) \hat{\sigma}_{fg} |0, g\rangle + e(x) \hat{\sigma}_{ef} |0, f\rangle], \end{aligned} \quad (9)$$

where $\varphi(x_1, x_2)$ is the two-phonon wave function. In addition, $f(x)$ is the wave function of one phonon with the other phonon absorbed by level $|f\rangle$, while $e(x)$ is the wave function of one phonon with the other phonon absorbed by $|e\rangle$. Substituting $|\psi\rangle$ into the stationary Schrödinger equation $\hat{H}_3|\psi\rangle = E|\psi\rangle$, one has

$$\begin{aligned} (-i\partial_{x_1} - i\partial_{x_2} - E)\varphi(x_1, x_2) \\ + \frac{V}{\sqrt{2}} [\delta(x_1)f(x_2) + \delta(x_2)f(x_1)] = 0, \end{aligned}$$

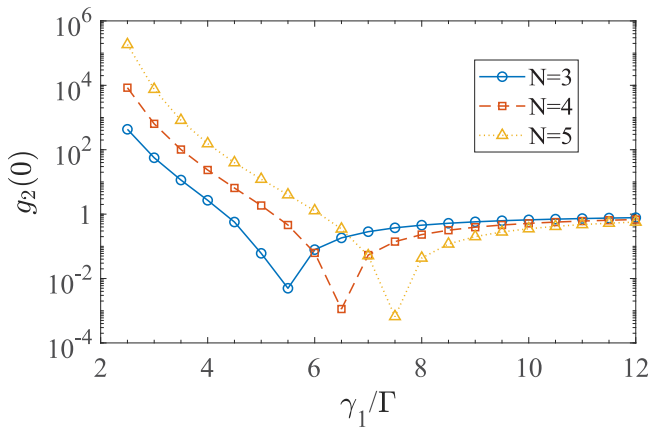


FIG. 5. Plot of $g_2(0)$ as a function of dissipation γ_1 for $N = 3, 4, 5$, with $\Delta = 0$.

$$\begin{aligned} (-i\partial_x + \omega_f - E)f(x) + \frac{V}{\sqrt{2}} [\varphi(0, x) \\ + \varphi(x, 0)] + \Omega e(x) = 0, \\ \left(-i\partial_x + \omega_e - \omega_0 - \frac{i\gamma_2}{2} - E \right) e(x) + \Omega f(x) = 0, \end{aligned} \quad (10)$$

where it is set to $\varphi(x, 0) = \varphi(0, x) = 1/2[\varphi(0^-, x) + \varphi(x, 0^+)]$ and $x_1 < x_2$. From Eq. (10), the boundary conditions for the two-phonon and single-phonon wave functions are

$$\begin{aligned} i[\varphi(x_1, 0^-) - \varphi(x_1, 0^+)] + \frac{Vf(x_1)}{\sqrt{2}} = 0, \\ i[\varphi(0^-, x_2) - \varphi(0^+, x_2)] + \frac{Vf(x_2)}{\sqrt{2}} = 0, \\ f(0^-) = f(0^+), \quad e(0^-) = e(0^+). \end{aligned} \quad (11)$$

Similar to the discussion in the preceding section, the two-phonon wave function can be described by $\varphi(x_1, x_2) = e^{iEr_c} G(r)$ ($r < 0$); the form of $G(r)$ is shown in Eq. (7). Substituting $\psi(x_1, x_2)$ into Eqs. (10) and (11), the relations among $G_{\text{in}}(r)$, $G_0(r)$, and $G_{\text{out}}(r)$ are given by

$$\begin{aligned} [\partial_r^2 + (\beta - \Gamma)\partial_r + \alpha + \xi]G_{\text{in}}(r) = (\partial_r^2 + \beta\partial_r + \alpha)G_0(r), \\ [\partial_r^2 - (\beta - \Gamma)\partial_r + \alpha + \xi]G_0(r) = (\partial_r^2 - \beta\partial_r + \alpha)G_{\text{out}}(r), \end{aligned} \quad (12)$$

where the parameters

$$\begin{aligned} \alpha = \Omega^2 + \left(i\delta + \frac{\gamma_2}{2} \right) \left(i\Delta + \frac{\Gamma}{2} \right), \\ \beta = i(\Delta + \delta) + \frac{\Gamma + \gamma_2}{2}, \\ \xi = -i\Gamma \left(\delta - i\frac{\gamma_2}{2} \right). \end{aligned} \quad (13)$$

The boundary conditions for $G(r)$ at $r = 0$ are

$$\begin{aligned} 2G_0(0) - G_{\text{in}}(0) = G_{\text{out}}(0), \\ \partial_r G_{\text{in}}(r)|_{r=0} + \Gamma[G_0(0) - G_{\text{in}}(0)] = \partial_r G_{\text{out}}(r)|_{r=0}. \end{aligned} \quad (14)$$

Equations (12) and (14) are sufficient to solve the chiral transport phonons scattered by a single SiV center. The output phonon states after the j th emitter are viewed as the input states for the $(j + 1)$ th emitter, and the transport phonons

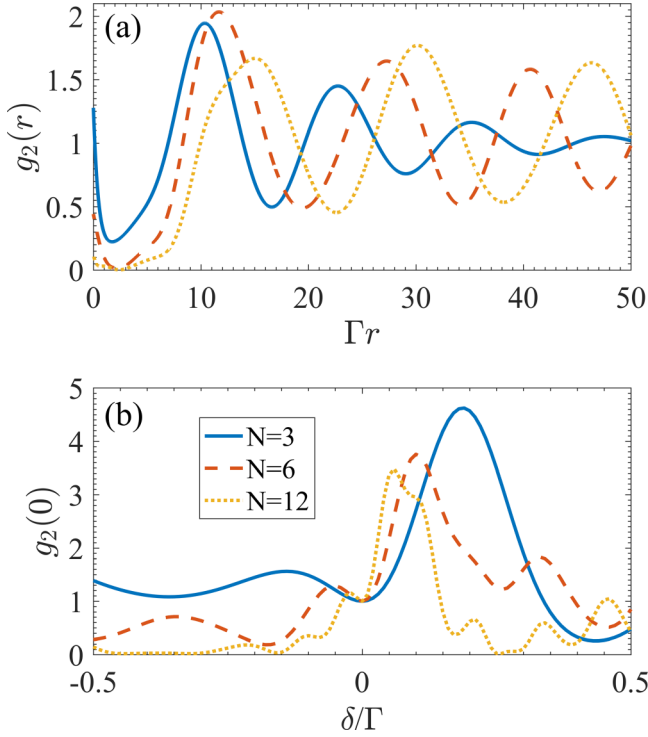


FIG. 6. (a) Second-order correlation function $g_2(r)$. Three cases of $N = 3, 6, 12$ are shown. (b) Plot of $g_2(0)$ versus various δ for different N . The parameters are $\Omega = 0.5\Gamma$ and $\Delta = -\delta = 0.25\Gamma$.

scattered by numerous SiV centers may be simply calculated. The positions of the SiV centers are labeled by r_j , with $j = 1, 2, \dots, N$. In this case, the phonon state amplitude $G(r)$ can be written as

$$G(r) = G_{i,j}(r), \quad r_i < x_1 < r_{i+1}, \quad r_j < x_2 < r_{j+1}, \quad (15)$$

where subscripts i and j denote that one phonon has passed through i emitters and the other through j emitters. We set $i \leq j$ due to $r = x_1 - x_2 < 0$, and $r_0 = -\infty$ and $r_{N+1} = +\infty$. It is assumed that the output amplitude of two phonons crossing j emitters is [71]

$$G_{j,j}(r) = T_j + \sum_{n=0}^{j-1} (A_{j,n} e^{\lambda_1 r} + B_{j,n} e^{\lambda_2 r}) \frac{r^n}{n!}, \quad (16)$$

where T_j , $A(B)_{j,n}$, and $\lambda_{1(2)}$ are constants to be determined. For two incoming phonons, we define $G_{0,0}(r) = T_0$, with T_0 a normalization constant. The details on how to obtain the final output after crossing N SiV centers are included in the Appendix. The resulting two-phonon correlation function can be characterized using the wave function obtained after crossing N SiV centers as

$$g_2(r) = \frac{|G_{N,N}(r)|^2}{|T_N|^2}; \quad (17)$$

here it is set to $T_0 = 1$.

The second-order correlation function $g_2(r)$ of the chiral transport phonons scattered by 3, 6, and 12 3LSCs is plotted in Fig. 6(a). Electromagnetic dissipation γ_2 is ignored in this case and the parameters are set at $\Omega = 0.5\Gamma$ and $\Delta = -\delta = 0.25\Gamma$. It is shown that as N increases, $g_2(0)$ decreases

from greater than unity to less than unity. That is, either two-phonon bunching states or antibunching states could be induced and greater N corresponds to stronger antibunching states. In contrast to the preceding section's results, the phononic antibunching states are successfully produced here without the necessity for significant phononic dissipations. When phonon-optical detuning changes, $g_2(0) < 1$ persists throughout a wide range of δ , as illustrated in Fig. 6(b). When $\delta = 0$, various amounts of N provide the same result of $g_2(0) = 1$, implying that effective phonon-phonon interactions do not arise once the chiral transport phonons are scattered by SiV centers.

To investigate phonon-phonon correlations on a large- N and $-\delta$ scale, Fig. 7(a) shows $g_2(0)$ versus various N and δ . For $\delta \neq 0$, a larger N corresponds to a smaller value of $g_2(0)$. The phononic antibunching states [$g_2(0) < 1$] appear in a broader range of δ as N increases, which is an expansion of the results in Fig. 6. In Figs. 7(c), 7(e), and 7(f), $g_2(0)$ is shown as a function of Δ and δ for $N = 10, 15$, and 20 , respectively. For various Δ and δ , phonon-phonon attractive or repulsive interactions are induced. Repulsive phonon-phonon interactions exist throughout a wider spectral range for greater N . This indicates that phonon-phonon interactions are tunable over a wide range of phonon frequencies. When $\delta = 0$, $g_2(0) \equiv 1$ for various N and Δ , which is marked by the red arrows in Figs. 7(b) and 7(d). The contour of $g_2(0) = 1$ is included in the figures.

Physical explanations of induced phonon bunching and antibunching states can be derived from the S matrix's composite eigenstates, as discussed in the preceding section. There are three sorts of two-phonon scattering eigenstates for input phonons interacting with a 3LSC [71]. In contrast to the delocalized eigenstate $|E\rangle_D$ and the bound eigenstate $|E\rangle_B$, the third eigenstate, called the scattering-resonance state (SRS) $|E\rangle_S$, comprises both delocalized and bound parts. The S matrix for phonons traversing N 3LSCs is $\hat{S} = \int dv [\lambda_D(v)^N |E\rangle_D \langle E| + \lambda_S(v)^N |E\rangle_S \langle E|] + \lambda_B^N |E\rangle_B \langle E|$, where $\lambda_{D,B,S}$ are the eigenvalues. The complex eigenvalues can be expressed as $\lambda \propto e^{i\phi}$. In Fig. 8 the three types of eigenstates are decomposed from the output two-phonon state $|\varphi_{\text{out}}\rangle$ for $N = 3$ [Fig. 8(a)], $N = 6$ [Fig. 8(b)], and $N = 12$ [Fig. 8(c)]. In contrast to the 2LSCs situation, when $r = 0$, the output two-phonon state is mostly impacted by the SRS (black dash-dotted line). With rising N , the eigenstates with continuous ν begin to dephase and the output state shifts from bunching to antibunching. The shape of $|\varphi_{\text{out}}(r)\rangle$ is similar to the second-order correlation function in Fig. 6(a) and it can also produce $g_2(r)$ when normalization is taken into account. The phenomenon $g_2(0) \equiv 1$ when $\delta = 0$ arises due to the electromagnetically induced transparency (EIT) [73], which destroys the nonlinearities of the 3LSCs and is incapable of inducing efficient phonon-phonon interactions.

For $N = 15$, the influence of laser parameters Ω and δ on $g_2(0)$ is investigated in Figs. 9(a), 9(c), and 9(d) for Δ equal to 0, 0.2Γ , and 0.4Γ , respectively. When $\delta = 0$, $g_2(0) \equiv 1$ for various laser Rabi frequencies, as seen by the red arrow in Fig. 9(b). When $\Delta = 0$, $g_2(0)$ in Fig. 9(a) performs symmetric properties about $\delta = 0$. In this situation, optical driving around the transition $|e\rangle \leftrightarrow |f\rangle$ is symmetric for $\pm\delta$ and the induced two-phonon interactions are identical for $\pm\delta$. When

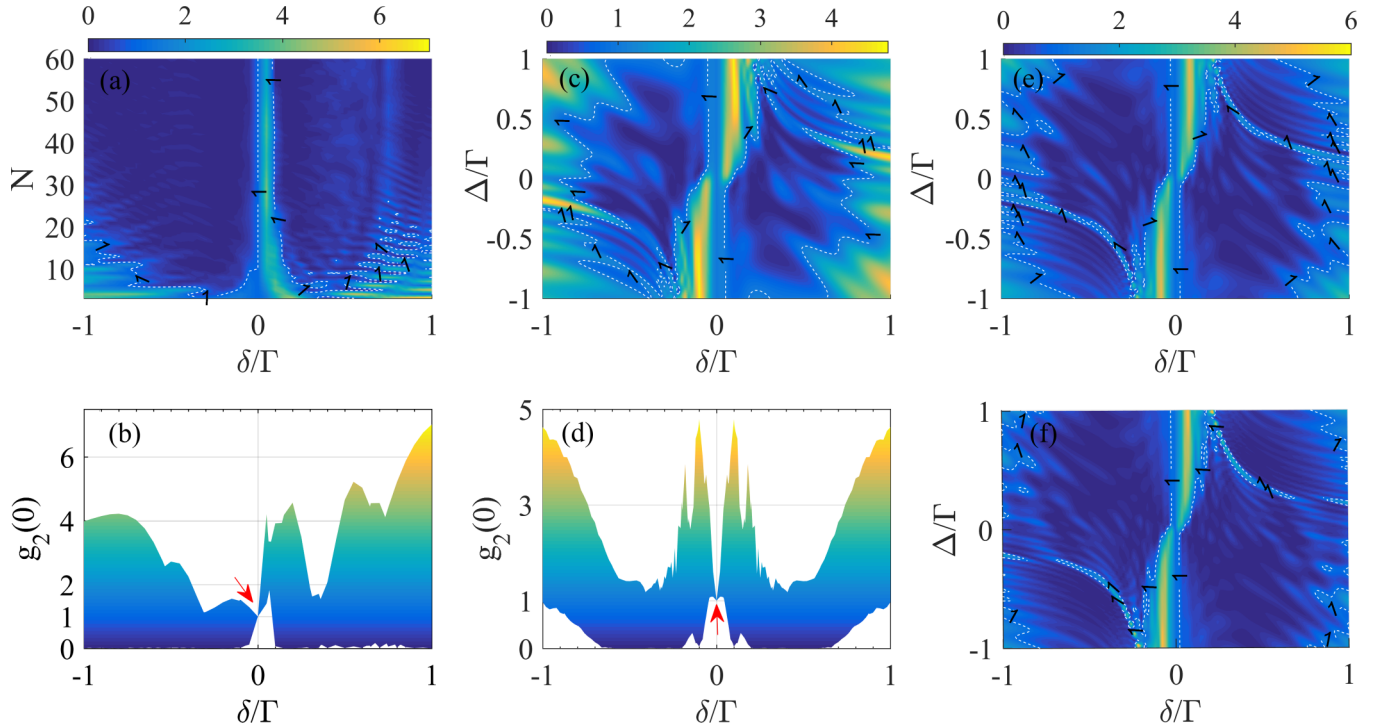


FIG. 7. (a) Plot of $g_2(0)$ as a function with N and δ . Also plotted is $g_2(0)$ versus Δ and δ for (c) $N = 10$, (e) $N = 15$, and (f) $N = 20$. (b) and (d) show the $X - Z$ view of (a) and (c), respectively. The red arrows denote $g_2(0) \equiv 1$ when $\delta = 0$. The parameters are the same as in Fig. 6.

$\Delta \neq 0$ and rises, the optical driving around the transition $|e\rangle \leftrightarrow |f\rangle$ for $\pm\delta$ becomes increasingly asymmetrical. The induced two-phonon interactions will then be asymmetrical for $\pm\delta$. As Ω rises, $g_2(0)$ tends to increase and transforms from less than 1 to greater than 1. The explanation for this phenomenon is that a larger Ω could result in a wider EIT window, which tends to diminish the nonlinearities of 3LSCs. For different laser parameters, we have $g_2(0) > 1$ or $g_2(0) < 1$ in the figure. This indicates that the laser Rabi frequency and detuning can control the phonon-phonon interactions of bunching or antibunching.

In the above discussion, the electromagnetic dissipation γ_2 from the excited level in 3LSCs is ignored. Figure 10 shows the effect of γ_2 on phonon-phonon interactions for different numbers of 3LSCs. When γ_2 is small, $g_2(0) < 1$ is unaffected; larger N corresponds to lower $g_2(0)$. As γ_2 increases, so does

$g_2(0)$, eventually becoming larger than unity for $N = 9, 12$. Larger N , on the other hand, correlates to greater phonon bunching states. More SiV centers would accrue higher electromagnetic dissipations, reducing system nonlinearities. As a result, the effects of N and γ_2 on inducing phonon antibunching states are competitive.

Comparing with the results of the phonon correlations created by 2LSCs in the preceding section, we show that the phonon antibunching can be achieved in 3LSCs without requiring substantial phononic dissipation. It is possible to accomplish either phonon antibunching or phonon bunching by manipulating external laser settings, i.e., the phonon-phonon interactions are tunable. Thus, 3LSCs are more effective in inducing repulsive phonon-phonon interactions, particularly adjustable phonon-phonon interactions.

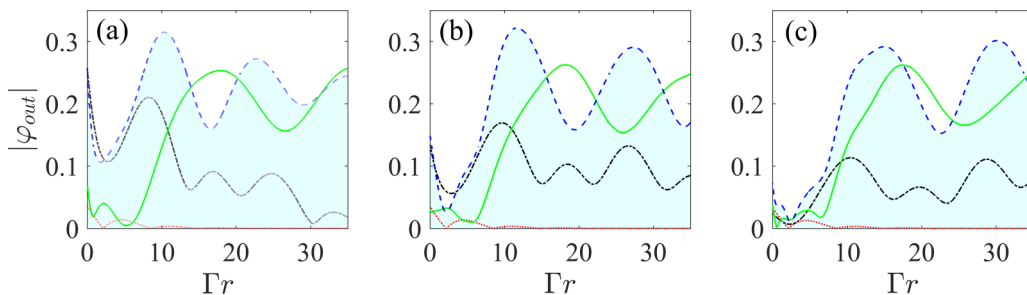


FIG. 8. Plot of $|\varphi_{out}(r)|$ (blue dashed line and shaded area) after being scattered by (a) 3, (b) 6, and (c) 12 3LSCs. Here $|\varphi_{out}(r)|$ is decomposed into three types of scattering eigenstates: a bound state (red dotted line), a delocalized state (green solid line), and a scattering-resonance state (black dash-dotted line). The parameters are the same as in Fig. 6.

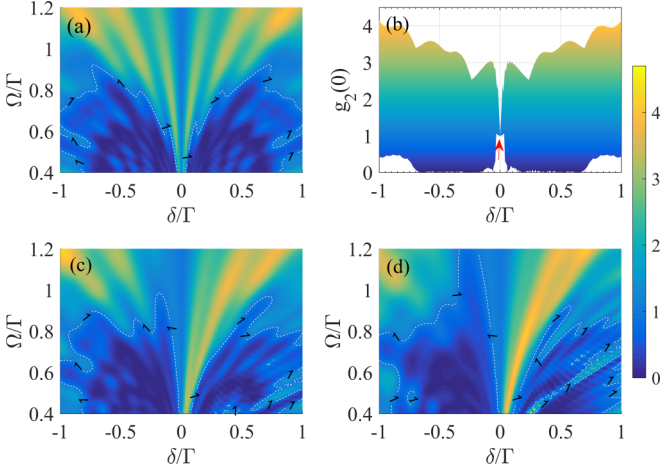


FIG. 9. Plot of $g_2(0)$ as a function of the laser parameters Ω and δ , with Δ set to (a) 0, (c) 0.2Γ , and (d) 0.4Γ . (b) shows the $X - Z$ view of (a). Red arrow denotes $g_2(0) \equiv 1$ when $\delta = 0$. Here N is set to 15.

V. EXPERIMENTAL FEASIBILITY

The experimental feasibility of the correlated phonons created by SiV centers in a 1D chiral acoustic waveguide is discussed in this section. The 1D chiral acoustic waveguide is inspired by Ref. [53], where the edge modes along the topological optomechanical crystal are used to transfer the quantum state between separated SiV centers. With phonon hopping rate $K = 2\pi \times 200$ MHz, photon hopping rate $J/K = 200$, and optomechanical coupling strength $G = 2K$, the chiral transport phonon velocity is $v_g \approx 1.4(aK)$, where a is the distance between the neighboring optomechanical cavities. A 1D chiral acoustic waveguide is produced along the edge of topological nanoelectromechanical lattice [54], optomechanical nanobeam lattice [44], and phononic metamaterials [56], according to several experiments. With the advancement of nanomechanical manufacturing technology, the 1D chiral acoustic waveguide coupling with SiV centers has a bright future. The probabilistic creation of one or two phonons using optomechanical interaction and a blue-

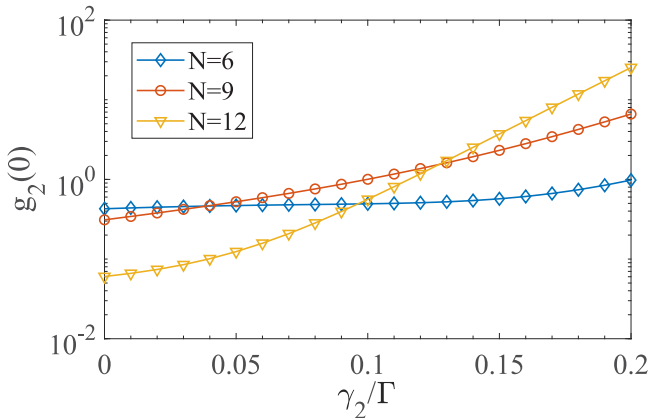


FIG. 10. Plot of $g_2(0)$ versus electromagnetic dissipation rate γ_2 for different N . The parameters are $\Omega = 0.6\Gamma$ and $\Delta = -\delta = 0.3\Gamma$.

detuned pulse has been reported [74,75]. A single-photon detector can be used to detect phonons, with mechanical excitations translated to an optical field through a red-detuned read pulse. Furthermore, similar to photonic systems [71,72], the few phonons can be created by mild mechanical actuation, with higher-order (greater than two) excitation terms being ignored. An optomechanical transducer might be used for optical excitation and phonon detection in optomechanical systems [76].

Ion implantation technologies can be used to create the implanted SiV centers [77–79]. Because phonon transmission is directional and multiple round-trip scattering between various centers is nonexistent, precise placements of SiV centers are not required in the work [71,72]. For the spin-phonon interaction constant $g = 0.2$ K [32], the phononic decay from SiV centers into guided modes is $\Gamma = a|V|^2/v_g \approx 2\pi \times 36$ MHz, which characterizes the phonon-phonon interaction strength [64]. At mK temperatures, the dephasing rate of SiV centers is about $\gamma_s \approx 2\pi \times 10^2$ Hz. The lifetime-limited linewidth of the excited state is roughly $\gamma_2 \approx 2\pi \times 39.8$ MHz at temperatures about 5 K [57,61], which is comparable to Γ . This seems disadvantageous for the discussion in this paper. Recently, much attention has been given to increasing the coherence time of ground levels in SiV centers, whose lifetime has been extended from approximately 100 ns to approximately 10 ms at a lower temperature of about 100 mK [63]. It has also been reported that the lifetime of the excited state is also related to the temperature [61,80]. Thus, increasing the excited-state lifetime may require further studies at low temperatures. In addition, increasing the strength of spin-phonon interactions is also a beneficial way to produce repulsive phonon-phonon interactions.

In practice, the waveguide's phonon modes would invariably be influenced by the external environment, resulting in an acoustic dissipation. The phononic Hamiltonian is modified to represent this noise as $\hat{H}_p = \sum_k [\omega_k - i(\bar{n} + 1)\gamma_k/2] \hat{b}_k^\dagger \hat{b}_k$, where $\gamma_k = \omega_k/Q$ is the acoustic dissipation rate, Q is the acoustic waveguide quality factor, and \bar{n} is the average number of thermal phonons. The number of the thermal phonon is $\bar{n} = 1/(e^{\hbar\omega/k_B T} - 1) \approx 0.047$ for the resonance scenario and temperature $T \approx 100$ mK, where k_B is the Boltzmann constant. When the stationary Schrödinger equation is solved with the modified Hamiltonian, the two-phonon wave function will have an exponential term $e^{-E\chi r_c}$, where $\chi = (\bar{n} + 1)/2Q$ and r_c is the center-of-mass coordinate. The amplitude of the two-phonon wave function will reduce to its $1/e$ after the phonons propagate around $33 \mu\text{m}$ when the acoustic quality factor is $Q \sim 10^7$. For $Q \sim 10^8$, the propagation distance of phonons can reach roughly $333 \mu\text{m}$ before the amplitude decreases to its $1/e$. The time spent on the efficient transport distance r_c/v_g is significantly less than the phonon lifetime Q/ω in the waveguide. Thus, for the higher acoustic quality factor, the phonons are able to travel further without causing considerable waveguide loss.

VI. SUMMARY

Strong tunable phonon-phonon interactions created by SiV centers were investigated in the 1D chiral phonon

waveguide. In the resonant scenario, odd numbers of 2LSCs induce phonon bunching correlations while even numbers have no effect on the transport phonons. When nonguided phonon dissipation from 2LSCs is considered, even numbers of 2LSCs start to induce phonon-phonon interactions. The phonon antibunching correlations are created under conditions of large phonon dissipation. However, phonon dissipation to the nonguided modes is so small that it is usually ignored. To achieve the phonon antibunching in a more feasible way, we introduced the 3LSCs to induce the phonon correlations. Results show that more SiV centers can induce stronger phonon antibunching states. Furthermore, the produced phonon-phonon interactions are controllable over a large phonon frequency range by manipulating the external laser Rabi frequency and detuning.

The scattering eigenstates of the spin-phonon interactions help explain the difference in induced phonon-phonon correlations between 2LSCs and 3LSCs systems [71,81]. Apart from delocalized and bound two-phonon states, the 3LSC system introduces a scattering-resonance state that plays an important role in the phonon characteristic scattering features. The strong tunable phonon-phonon interactions may contribute to the advancements of solid acoustic quantum information processing, such as the creation of single phonons and self-organization acoustic phenomena at the quantum level [81].

ACKNOWLEDGMENTS

This work was supported by the National Natural Science Foundation of China under Grant No. 92065105 and the Natural Science Basic Research Program of Shaanxi (Program No. 2020JC-02).

APPENDIX: SECOND-ORDER CORRELATION FUNCTION FOR PHONONS SCATTERED BY MULTIPLE SiV CENTERS

In the main text, it was shown that the output phonon state after being scattered by one SiV center can be solved from Eqs. (12) and (14). This Appendix contains the complete solution procedure for obtaining the output phonon wave functions after scattering by N SiV centers, as well as the corresponding second-order correlation functions. Note that the solution for output phonon states scattered by 2LSCs is a simplified version of the process for 3LSCs, which will be discussed later.

Following Ref. [71], the two-phonon wave function $G_{j,j}(r)$ scattered by 3LSCs obeys the recursion relation

$$\dots \rightarrow G_{j,j}(r) \rightarrow G_{j,j+1}(r) \rightarrow G_{j+1,j+1}(r) \rightarrow \dots \quad (A1)$$

It allows one to determine the output phonon state after traversing N 3LSCs. The expression of $G_{j,j}(r)$ is shown in Eq. (16), where λ_1 and λ_2 are the solutions of the function $\lambda^2 - \beta\lambda + \alpha = 0$. With Eqs. (A1) and (12) one has

$$[\partial_r^2 + (\beta - \Gamma)\partial_r + \alpha + \xi]G_{j,j}(r) = (\partial_r^2 + \beta\partial_r + \alpha)G_{j,j+1}(r), \quad (A2)$$

$$[\partial_r^2 - (\beta - \Gamma)\partial_r + \alpha + \xi]G_{j,j+1}(r) = (\partial_r^2 - \beta\partial_r + \alpha)G_{j+1,j+1}(r), \quad (A3)$$

where β , α , and ξ are the parameters given in Eq. (13). Substituting Eq. (16) into Eq. (A2), the function regarding $G_{j,j+1}(r)$ is

$$\begin{aligned} (\partial_r^2 + \beta\partial_r + \alpha)G_{j,j+1} &= (\alpha + \xi)T_j + \sum_{n=0}^{j-1} (n_1A_{j,n}e^{\lambda_1 r} + n_2B_{j,n}e^{\lambda_2 r}) \frac{r^n}{n!} + \sum_{n=1}^{j-1} (n_3A_{j,n}e^{\lambda_1 r} + n_4B_{j,n}e^{\lambda_2 r}) \frac{r^{n-1}}{(n-1)!} \\ &+ \sum_{n=2}^{j-1} (A_{j,n}e^{\lambda_1 r} + B_{j,n}e^{\lambda_2 r}) \frac{r^{n-2}}{(n-2)!}, \end{aligned} \quad (A4)$$

where

$$n_1 = (2\beta - \Gamma)\lambda_1 + \xi, \quad n_2 = (2\beta - \Gamma)\lambda_2 + \xi, \quad n_3 = 2\lambda_1 + \beta - \Gamma, \quad n_4 = 2\lambda_2 + \beta - \Gamma.$$

According to the form of $G_{j,j}(r)$ in Eq. (16), the solution to Eq. (A4) is expressed as

$$G_{j,j+1}(r) = \mathcal{T}_j + \sum_{n=0}^{j-1} (\mathcal{A}_{j,n}e^{\lambda_1 r} + \mathcal{B}_{j,n}e^{\lambda_2 r}) \frac{r^n}{n!}. \quad (A5)$$

After substituting Eq. (A5) into Eq. (A4), one has $\mathcal{T}_j = T_j(\alpha + \xi)/\alpha$ and

$$\begin{aligned} 2\beta\lambda_1\mathcal{A}_{j,j-1} &= n_1\mathcal{A}_{j,j-1}, \\ 2\beta\lambda_2\mathcal{B}_{j,j-1} &= n_2\mathcal{B}_{j,j-1}, \\ 2\beta\lambda_1\mathcal{A}_{j,j-2} + n_5\mathcal{A}_{j,j-1} &= n_1\mathcal{A}_{j,j-2} + n_3\mathcal{A}_{j,j-1}, \\ 2\beta\lambda_2\mathcal{B}_{j,j-2} + n_6\mathcal{B}_{j,j-1} &= n_2\mathcal{B}_{j,j-2} + n_4\mathcal{B}_{j,j-1}, \\ 2\beta\lambda_1\mathcal{A}_{j,n} + n_5\mathcal{A}_{j,n+1} + \mathcal{A}_{j,n+2} &= n_1\mathcal{A}_{j,n} + n_3\mathcal{A}_{j,n+1} + \mathcal{A}_{j,n+2}, \\ 2\beta\lambda_2\mathcal{B}_{j,n} + n_6\mathcal{B}_{j,n+1} + \mathcal{B}_{j,n+2} &= n_2\mathcal{B}_{j,n} + n_4\mathcal{B}_{j,n+1} + \mathcal{B}_{j,n+2}, \end{aligned} \quad (A6)$$

where $n_5 = 2\lambda_1 + \beta$, $n_6 = 2\lambda_2 + \beta$, and the subscripts of $A(B)_{i,j}$ and $\mathcal{A}(\mathcal{B})_{i,j}$ obey $i > j \geq 0$.

Similarly, the function about $G_{j+1,j+1}$ can be obtained by substituting Eq. (A5) into Eq. (A3) as

$$\begin{aligned} (\partial_r^2 - \beta\partial_r + \alpha)G_{j+1,j+1} &= (\alpha + \xi)\mathcal{T}_j + \sum_{n=0}^{j-1} (m_1\mathcal{A}_{j,n}e^{\lambda_1 r} + m_2\mathcal{B}_{j,n}e^{\lambda_2 r})\frac{r^n}{n!} \\ &+ \sum_{n=1}^{j-1} (m_3\mathcal{A}_{j,n}e^{\lambda_1 r} + m_4\mathcal{B}_{j,n}e^{\lambda_2 r})\frac{r^{n-1}}{(n-1)!} + \sum_{n=2}^{j-1} (\mathcal{A}_{j,n}e^{\lambda_1 r} + \mathcal{B}_{j,n}e^{\lambda_2 r})\frac{r^{n-2}}{(n-2)!}, \end{aligned} \quad (\text{A7})$$

where

$$m_1 = \xi + \Gamma\lambda_1, \quad m_2 = \xi + \Gamma\lambda_2, \quad m_3 = 2\lambda_1 - \beta + \Gamma, \quad m_4 = 2\lambda_2 - \beta + \Gamma.$$

According to Eq. (16), $G_{j+1,j+1}$ is described by

$$G_{j+1,j+1}(r) = T_{j+1} + \sum_{n=0}^j (\mathcal{A}_{j+1,n}e^{\lambda_1 r} + \mathcal{B}_{j+1,n}e^{\lambda_2 r})\frac{r^n}{n!}. \quad (\text{A8})$$

Substituting Eq. (A8) into Eq. (A7), one has $T_{j+1} = T_j(\alpha + \xi)^2/\alpha^2$ and

$$\begin{aligned} m_5\mathcal{A}_{j+1,j} &= m_1\mathcal{A}_{j,j-1}, \\ m_6\mathcal{B}_{j+1,j} &= m_2\mathcal{B}_{j,j-1}, \\ m_5\mathcal{A}_{j+1,j-1} + \mathcal{A}_{j+1,j} &= m_1\mathcal{A}_{j,j-2} + m_3\mathcal{A}_{j,j-1}, \\ m_6\mathcal{B}_{j+1,j-1} + \mathcal{B}_{j+1,j} &= m_2\mathcal{B}_{j,j-2} + m_4\mathcal{B}_{j,j-1}, \\ m_5\mathcal{A}_{j+1,n} + \mathcal{A}_{j+1,n+1} &= m_1\mathcal{A}_{j,n-1} + m_3\mathcal{A}_{j,n} + \mathcal{A}_{j,n+1}, \\ m_6\mathcal{B}_{j+1,n} + \mathcal{B}_{j+1,n+1} &= m_2\mathcal{B}_{j,n-1} + m_4\mathcal{B}_{j,n} + \mathcal{B}_{j,n+1}, \end{aligned} \quad (\text{A9})$$

where $m_5 = 2\lambda_1 - \beta$, $m_6 = 2\lambda_2 - \beta$, and the subscripts of $\mathcal{A}(\mathcal{B})_{i,j}$ and $\mathcal{A}(\mathcal{B})_{i,j}$ obey $i > j \geq 0$.

To obtain $G_{N,N}(r)$ from the initial phonon amplitude $G_{0,0}(r)$, the two parameters $\mathcal{A}_{j+1,0}$ and $\mathcal{B}_{j+1,0}$ are lacking. So far, the boundary conditions have not been used, and $\mathcal{A}_{j+1,0}$ and $\mathcal{B}_{j+1,0}$ can be derived from Eq. (14), which gives

$$\begin{aligned} \mathcal{A}_{j+1,0} + \mathcal{B}_{j+1,0} &= -T_j\frac{\xi^2}{\alpha^2} + 2(\mathcal{A}_{j,0} + \mathcal{B}_{j,0}) - \mathcal{A}_{j,0} - \mathcal{B}_{j,0}, \end{aligned}$$

$$\begin{aligned} \lambda_1\mathcal{A}_{j+1,0} + \lambda_2\mathcal{B}_{j+1,0} &= T_j\Gamma\frac{\xi}{\alpha} + \Gamma(\mathcal{A}_{j,0} + \mathcal{B}_{j,0}) + (\lambda_1 - \Gamma)\mathcal{A}_{j,0} \\ &+ (\lambda_2 - \Gamma)\mathcal{B}_{j,0} + \mathcal{A}_{j,1} + \mathcal{B}_{j,1} - \mathcal{A}_{j+1,1} - \mathcal{B}_{j+1,1}. \end{aligned} \quad (\text{A10})$$

With the recursion relation in Eqs. (16), (A6), (A9), and (A10) and the initial input phonon state, the two-phonon output state amplitude $G_{N,N}(r)$ can be solved successfully. For $T_0 = 1$, one can acquire $T_N = (\alpha + \xi)^2/\alpha^2$ and the two-phonon correlation function $g_2(r) = |G_{N,N}(r)|^2/|T_N|^2$.

The above procedure can also be used to calculate the second-order correlation function for the output phonon state after it has been scattered by 2LSCs. Because chiral transport phonons interact with 2LSCs, the laser Rabi frequency and phonon-optical detuning must be adjusted to zero. The energy of the excited level should also be set to zero. As a result, the parameters in Eq. (13) become

$$\begin{aligned} \alpha &= -i\omega\left(i\Delta + \frac{\gamma_1 + \Gamma}{2}\right), \\ \beta &= i(\Delta - \omega) + \frac{\Gamma + \gamma_1}{2}, \\ \xi &= i\Gamma\omega, \end{aligned} \quad (\text{A11})$$

where ω is the phonon frequency and γ_1 is the phonon dissipation from 2LSCs to nonguided modes. The phonon correlations caused by 2LSCs can be determined from the aforementioned calculation methods using these modified parameters.

-
- [1] A. Wallraff, D. I. Schuster, A. Blais, L. Frunzio, R.-S. Huang, J. Majer, S. Kumar, S. M. Girvin, and R. J. Schoelkopf, Strong coupling of a single photon to a superconducting qubit using circuit quantum electrodynamics, *Nature (London)* **431**, 162 (2004).
- [2] A. Clerk, K. Lehnert, P. Bertet, J. Petta, and Y. Nakamura, Hybrid quantum systems with circuit quantum electrodynamics, *Nat. Phys.* **16**, 257 (2020).
- [3] A. Blais, S. M. Girvin, and W. D. Oliver, Quantum information processing and quantum optics with circuit quantum electrodynamics, *Nat. Phys.* **16**, 247 (2020).
- [4] J. Teissier, A. Barfuss, P. Appel, E. Neu, and P. Maletinsky, Strain Coupling of a Nitrogen-Vacancy Center Spin to a Diamond Mechanical Oscillator, *Phys. Rev. Lett.* **113**, 020503 (2014).
- [5] D. Lee, K. W. Lee, J. V. Cady, P. Ouartchaiyapong, and A. C. B. Jayich, Topical review: Spins and mechanics in diamond, *J. Opt.* **19**, 033001 (2017).
- [6] J. Chan, T. M. Alegre, A. H. Safavi-Naeini, J. T. Hill, A. Krause, S. Gröblacher, M. Aspelmeyer, and O. Painter, Laser cooling of a nanomechanical oscillator into its quantum ground state, *Nature (London)* **478**, 89 (2011).
- [7] J. D. Jost, J. Home, J. M. Amini, D. Hanneke, R. Ozeri, C. Langer, J. J. Bollinger, D. Leibfried, and D. J. Wineland, Entangled mechanical oscillators, *Nature (London)* **459**, 683 (2009).
- [8] E. Rosenfeld, R. Riedinger, J. Gieseler, M. Schuetz, and M. D. Lukin, Efficient Entanglement of Spin Qubits Mediated by a Hot Mechanical Oscillator, *Phys. Rev. Lett.* **126**, 250505 (2021).

- [9] Y. Tabuchi, S. Ishino, A. Noguchi, T. Ishikawa, R. Yamazaki, K. Usami, and Y. Nakamura, Coherent coupling between a ferromagnetic magnon and a superconducting qubit, *Science* **349**, 405 (2015).
- [10] A. V. Chumak, V. I. Vasyuchka, A. A. Serga, and B. Hillebrands, Magnon spintronics, *Nat. Phys.* **11**, 453 (2015).
- [11] T. Nomura, X.-X. Zhang, S. Zherlitsyn, J. Wosnitza, Y. Tokura, N. Nagaosa, and S. Seki, Phonon Magneto-chiral Effect, *Phys. Rev. Lett.* **122**, 145901 (2019).
- [12] T. Kikkawa, K. Shen, B. Flebus, R. A. Duine, K.-i. Uchida, Z. Qiu, G. E. W. Bauer, and E. Saitoh, Magnon Polarons in the Spin Seebeck Effect, *Phys. Rev. Lett.* **117**, 207203 (2016).
- [13] J. Holanda, D. Maior, A. Azevedo, and S. Rezende, Detecting the phonon spin in magnon-phonon conversion experiments, *Nat. Phys.* **14**, 500 (2018).
- [14] C. Kong, H. Xiong, and Y. Wu, Magnon-Induced Nonreciprocity Based on the Magnon Kerr Effect, *Phys. Rev. Applied* **12**, 034001 (2019).
- [15] R. Hanson and D. D. Awschalom, Coherent manipulation of single spins in semiconductors, *Nature (London)* **453**, 1043 (2008).
- [16] M. W. Doherty, N. B. Manson, P. Delaney, F. Jelezko, J. Wrachtrup, and L. C. Hollenberg, The nitrogen-vacancy colour centre in diamond, *Phys. Rep.* **528**, 1 (2013).
- [17] D. A. Golter, T. Oo, M. Amezcua, I. Lekavicius, K. A. Stewart, and H. Wang, Coupling a Surface Acoustic Wave to an Electron Spin in Diamond via a Dark State, *Phys. Rev. X* **6**, 041060 (2016).
- [18] P. Rabl, S. J. Kolkowitz, F. H. L. Koppens, J. G. E. Harris, P. Zoller, and M. D. Lukin, A quantum spin transducer based on nanoelectromechanical resonator arrays, *Nat. Phys.* **6**, 602 (2010).
- [19] Y. Zhou, A. Rasmita, K. Li, Q. Xiong, I. Aharonovich, and W.-b. Gao, Coherent control of a strongly driven silicon vacancy optical transition in diamond, *Nat. Commun.* **8**, 14451 (2017).
- [20] L. J. Rogers, O. Wang, Y. Liu, L. Antoniuk, C. Osterkamp, V. A. Davydov, V. N. Agafonov, A. B. Filipovski, F. Jelezko, and A. Kubanek, Single Si - V⁻ Centers in Low-Strain Nanodiamonds with Bulklike Spectral Properties and Nanomanipulation Capabilities, *Phys. Rev. Applied* **11**, 024073 (2019).
- [21] C. Weinzettl, J. Görlitz, J. N. Becker, I. A. Walmsley, E. Poem, J. Nunn, and C. Becher, Coherent Control and Wave Mixing in an Ensemble of Silicon-Vacancy Centers in Diamond, *Phys. Rev. Lett.* **122**, 063601 (2019).
- [22] Z.-L. Xiang, S. Ashhab, J. Q. You, and F. Nori, Hybrid quantum circuits: Superconducting circuits interacting with other quantum systems, *Rev. Mod. Phys.* **85**, 623 (2013).
- [23] G. Kurizki, P. Bertet, Y. Kubo, K. Mølmer, D. Petrosyan, P. Rabl, and J. Schmiedmayer, Quantum technologies with hybrid systems, *Proc. Natl. Acad. Sci. USA* **112**, 3866 (2015).
- [24] D. Lachance-Quirion, Y. Tabuchi, A. Glorpe, K. Usami, and Y. Nakamura, Hybrid quantum systems based on magnonics, *Appl. Phys. Express* **12**, 070101 (2019).
- [25] S. D. Bennett, N. Y. Yao, J. Otterbach, P. Zoller, P. Rabl, and M. D. Lukin, Phonon-Induced Spin-Spin Interactions in Diamond Nanostructures: Application to Spin Squeezing, *Phys. Rev. Lett.* **110**, 156402 (2013).
- [26] Y.-F. Qiao, H.-Z. Li, X.-L. Dong, J.-Q. Chen, Y. Zhou, and P.-B. Li, Phononic-waveguide-assisted steady-state entanglement of silicon-vacancy centers, *Phys. Rev. A* **101**, 042313 (2020).
- [27] X.-X. Li, B. Li, and P.-B. Li, Simulation of topological phases with color center arrays in phononic crystals, *Phys. Rev. Research* **2**, 013121 (2020).
- [28] X.-X. Li, P.-B. Li, H.-R. Li, H. Gao, and F.-L. Li, Simulation of topological Zak phase in spin-phononic crystal networks, *Phys. Rev. Research* **3**, 013025 (2021).
- [29] J. Li, S.-Y. Zhu, and G. S. Agarwal, Magnon-Photon-Phonon Entanglement in Cavity Magnomechanics, *Phys. Rev. Lett.* **121**, 203601 (2018).
- [30] J. Li, S. Y. Zhu, and G. S. Agarwal, Squeezed states of magnons and phonons in cavity magnomechanics, *Phys. Rev. A* **99**, 021801(R) (2019).
- [31] S. Meesala, Y.-I. Sohn, B. Pingault, L. Shao, H. A. Atikian, J. Holzgrafe, M. Gündoğan, C. Stavrakas, A. Sipahigil, C. Chia, R. Evans, M. J. Burek, M. Zhang, L. Wu, J. L. Pacheco, J. Abraham, E. Bielejec, M. D. Lukin, M. Atatüre, and M. Lončar, Strain engineering of the silicon-vacancy center in diamond, *Phys. Rev. B* **97**, 205444 (2018).
- [32] M.-A. Lemonde, S. Meesala, A. Sipahigil, M. J. A. Schuetz, M. D. Lukin, M. Loncar, and P. Rabl, Phonon Networks with Silicon-Vacancy Centers in Diamond Waveguides, *Phys. Rev. Lett.* **120**, 213603 (2018).
- [33] M. V. Gustafsson, T. Aref, A. F. Kockum, M. K. Ekström, G. Johansson, and P. Delsing, Propagating phonons coupled to an artificial atom, *Science* **346**, 207 (2014).
- [34] T. Ramos, V. Sudhir, K. Stannigel, P. Zoller, and T. J. Kippenberg, Nonlinear Quantum Optomechanics via Individual Intrinsic Two-Level Defects, *Phys. Rev. Lett.* **110**, 193602 (2013).
- [35] X. Wang, A. Miranowicz, H.-R. Li, and F. Nori, Method for observing robust and tunable phonon blockade in a nanomechanical resonator coupled to a charge qubit, *Phys. Rev. A* **93**, 063861 (2016).
- [36] H. Xie, C.-G. Liao, X. Shang, Z.-H. Chen, and X.-M. Lin, Optically induced phonon blockade in an optomechanical system with second-order nonlinearity, *Phys. Rev. A* **98**, 023819 (2018).
- [37] L.-L. Zheng, T.-S. Yin, Q. Bin, X.-Y. Lü, and Y. Wu, Single-photon-induced phonon blockade in a hybrid spin-optomechanical system, *Phys. Rev. A* **99**, 013804 (2019).
- [38] T.-S. Yin, Q. Bin, G.-L. Zhu, G.-R. Jin, and A. Chen, Phonon blockade in a hybrid system via the second-order magnetic gradient, *Phys. Rev. A* **100**, 063840 (2019).
- [39] J. Tang, Y. Wu, Z. Wang, H. Sun, L. Tang, H. Zhang, T. Li, Y. Lu, M. Xiao, and K. Xia, Vacuum-induced surface-acoustic-wave phonon blockade, *Phys. Rev. A* **101**, 053802 (2020).
- [40] P. Wang, L. Lu, and K. Bertoldi, Topological Phononic Crystals with One-Way Elastic Edge Waves, *Phys. Rev. Lett.* **115**, 104302 (2015).
- [41] Y. Wang, B. Yousefzadeh, H. Chen, H. Nassar, G. Huang, and C. Daraio, Observation of Nonreciprocal Wave Propagation in a Dynamic Phononic Lattice, *Phys. Rev. Lett.* **121**, 194301 (2018).
- [42] A. Seif, W. DeGottardi, K. Esfarjani, and M. Hafezi, Thermal management and non-reciprocal control of phonon flow via optomechanics, *Nat. Commun.* **9**, 1207 (2018).
- [43] H. Xu, L. Jiang, A. Clerk, and J. Harris, Nonreciprocal control and cooling of phonon modes in an optomechanical system, *Nature (London)* **568**, 65 (2019).

- [44] J. P. Mathew, J. Del Pino, and E. Verhagen, Synthetic gauge fields for phonon transport in a nano-optomechanical system, *Nat. Nanotechnol.* **15**, 198 (2020).
- [45] S. Liu, Z.-q. Yin, and T. Li, Prethermalization and nonreciprocal phonon transport in a levitated optomechanical array, *Adv. Quantum Technol.* **3**, 1900099 (2020).
- [46] Y.-B. Qian, D.-G. Lai, M.-R. Chen, and B.-P. Hou, Non-reciprocal photon transmission with quantum noise reduction via cross-Kerr nonlinearity, *Phys. Rev. A* **104**, 033705 (2021).
- [47] C. Sanavio, V. Peano, and A. Xuereb, Nonreciprocal topological phononics in optomechanical arrays, *Phys. Rev. B* **101**, 085108 (2020).
- [48] X.-L. Dong, P.-B. Li, T. Liu, and F. Nori, Unconventional Quantum Sound-Matter Interactions in Spin-Optomechanical-Crystal Hybrid Systems, *Phys. Rev. Lett.* **126**, 203601 (2021).
- [49] H. Xie, C.-G. Liao, X. Shang, M.-Y. Ye, and X.-M. Lin, Phonon blockade in a quadratically coupled optomechanical system, *Phys. Rev. A* **96**, 013861 (2017).
- [50] Y. Wang, J.-L. Wu, J.-X. Han, Y. Xia, Y.-Y. Jiang, and J. Song, Enhanced Phonon Blockade in a Weakly Coupled Hybrid System via Mechanical Parametric Amplification, *Phys. Rev. Applied* **17**, 024009 (2022).
- [51] C.-P. Shen, X.-L. Dong, J.-Q. Chen, Y.-F. Qiao, and P.-B. Li, Strong two-phonon correlations and bound states in the continuum in phononic waveguides with embedded six centers, *Adv. Quantum Technol.* **4**, 2100074 (2021).
- [52] C. Brendel, V. Peano, O. Painter, and F. Marquardt, Snowflake phononic topological insulator at the nanoscale, *Phys. Rev. B* **97**, 020102(R) (2018).
- [53] M.-A. Lemonde, V. Peano, P. Rabl, and D. G. Angelakis, Quantum state transfer via acoustic edge states in a 2D optomechanical array, *New J. Phys.* **21**, 113030 (2019).
- [54] J. Cha, K. W. Kim, and C. Daraio, Experimental realization of on-chip topological nanoelectromechanical metamaterials, *Nature (London)* **564**, 229 (2018).
- [55] V. Peano, C. Brendel, M. Schmidt, and F. Marquardt, Topological Phases of Sound and Light, *Phys. Rev. X* **5**, 031011 (2015).
- [56] S. H. Mousavi, A. B. Khanikaev, and Z. Wang, Topologically protected elastic waves in phononic metamaterials, *Nat. Commun.* **6**, 8682 (2015).
- [57] E. Neu, C. Hepp, M. Hauschild, S. Gsell, M. Fischer, H. Sternschulte, D. Steinmüller-Nethl, M. Schreck, and C. Becher, Low-temperature investigations of single silicon vacancy colour centres in diamond, *New J. Phys.* **15**, 043005 (2013).
- [58] C. Hepp, T. Müller, V. Waselowski, J. N. Becker, B. Pingault, H. Sternschulte, D. Steinmüller-Nethl, A. Gali, J. R. Maze, M. Atatüre, and C. Becher, Electronic Structure of the Silicon Vacancy Color Center in Diamond, *Phys. Rev. Lett.* **112**, 036405 (2014).
- [59] A. Dietrich, K. D. Jahnke, J. M. Binder, T. Teraji, J. Isoya, L. J. Rogers, and F. Jelezko, Isotopically varying spectral features of silicon-vacancy in diamond, *New J. Phys.* **16**, 113019 (2014).
- [60] L. J. Rogers, K. D. Jahnke, M. H. Metsch, A. Sipahigil, J. M. Binder, T. Teraji, H. Sumiya, J. Isoya, M. D. Lukin, P. Hemmer, and F. Jelezko, All-Optical Initialization, Readout, and Coherent Preparation of Single Silicon-Vacancy Spins in Diamond, *Phys. Rev. Lett.* **113**, 263602 (2014).
- [61] K. D. Jahnke, A. Sipahigil, J. M. Binder, M. W. Doherty, M. Metsch, L. J. Rogers, N. B. Manson, M. D. Lukin, and F. Jelezko, Electron-phonon processes of the silicon-vacancy centre in diamond, *New J. Phys.* **17**, 043011 (2015).
- [62] R. E. Evans, A. Sipahigil, D. D. Sukachev, A. S. Zibrov, and M. D. Lukin, Narrow-Linewidth Homogeneous Optical Emitters in Diamond Nanostructures via Silicon Ion Implantation, *Phys. Rev. Applied* **5**, 044010 (2016).
- [63] D. D. Sukachev, A. Sipahigil, C. T. Nguyen, M. K. Bhaskar, R. E. Evans, F. Jelezko, and M. D. Lukin, Silicon-Vacancy Spin Qubit in Diamond: A Quantum Memory Exceeding 10 ms with Single-Shot State Readout, *Phys. Rev. Lett.* **119**, 223602(R) (2017).
- [64] D. Roy, C. M. Wilson, and O. Firstenberg, *Colloquium: Strongly interacting photons in one-dimensional continuum*, *Rev. Mod. Phys.* **89**, 021001 (2017).
- [65] J. Shen and S. Fan, Coherent photon transport from spontaneous emission in one-dimensional waveguides., *Opt. Lett.* **30**, 2001 (2005).
- [66] J.-T. Shen and S. Fan, Coherent Single Photon Transport in a One-Dimensional Waveguide Coupled with Superconducting Quantum Bits, *Phys. Rev. Lett.* **95**, 213001 (2005).
- [67] J.-T. Shen and S. Fan, Strongly Correlated Two-Photon Transport in a One-Dimensional Waveguide Coupled to a Two-Level System, *Phys. Rev. Lett.* **98**, 153003 (2007).
- [68] J.-T. Shen and S. Fan, Strongly correlated multiparticle transport in one dimension through a quantum impurity, *Phys. Rev. A* **76**, 062709 (2007).
- [69] H. Zheng, D. J. Gauthier, and H. U. Baranger, Cavity-Free Photon Blockade Induced by Many-Body Bound States, *Phys. Rev. Lett.* **107**, 223601 (2011).
- [70] H. Zheng, D. J. Gauthier, and H. U. Baranger, Strongly correlated photons generated by coupling a three- or four-level system to a waveguide, *Phys. Rev. A* **85**, 043832 (2012).
- [71] O. A. Iversen and T. Pohl, Strongly Correlated States of Light and Repulsive Photons in Chiral Chains of Three-Level Quantum Emitters, *Phys. Rev. Lett.* **126**, 083605 (2021).
- [72] S. Mahmoodian, M. Čepulkovskis, S. Das, P. Lodahl, K. Hammerer, and A. S. Sørensen, Strongly Correlated Photon Transport in Waveguide Quantum Electrodynamics with Weakly Coupled Emitters, *Phys. Rev. Lett.* **121**, 143601 (2018).
- [73] M. Fleischhauer, A. Imamoglu, and J. P. Marangos, Electromagnetically induced transparency: Optics in coherent media, *Rev. Mod. Phys.* **77**, 633 (2005).
- [74] R. Riedinger, S. Hong, R. A. Norte, J. A. Slater, J. Shang, A. G. Krause, V. Anant, M. Aspelmeyer, and S. Gröblacher, Non-classical correlations between single photons and phonons from a mechanical oscillator, *Nature (London)* **530**, 313 (2016).
- [75] S. Hong, R. Riedinger, I. Marinković, A. Wallucks, S. G. Hofer, R. A. Norte, M. Aspelmeyer, and S. Gröblacher, Hanbury Brown and Twiss interferometry of single phonons from an optomechanical resonator, *Science* **358**, 203 (2017).
- [76] R. N. Patel, Z. Wang, W. Jiang, C. J. Sarabalis, J. T. Hill, and A. H. Safavi-Naeini, Single-Mode Phononic Wire, *Phys. Rev. Lett.* **121**, 040501 (2018).
- [77] J. Wang, Y. Zhou, X. Zhang, F. Liu, Y. Li, K. Li, Z. Liu, G. Wang, and W. Gao, Efficient Generation of an Array of Single Silicon-Vacancy Defects in Silicon Carbide, *Phys. Rev. Applied* **7**, 064021 (2017).

- [78] C. Bradac, W. Gao, J. Forneris, M. E. Trusheim, and I. Aharonovich, Quantum nanophotonics with group IV defects in diamond, *Nat. Commun.* **10**, 5625 (2019).
- [79] D. M. Toyli, C. D. Weis, G. D. Fuchs, T. Schenkel, and D. D. Awschalom, Chip-scale nanofabrication of single spins and spin arrays in diamond, *Nano Lett.* **10**, 3168 (2010).
- [80] F. Lenzini, N. Gruhler, N. Walter, and W. H. Pernice, Diamond as a platform for integrated quantum photonics, *Adv. Quantum Technol.* **1**, 1800061 (2018).
- [81] O. A. Iversen and T. Pohl, Self-ordering of individual photons in waveguide QED and Rydberg-atom arrays, *Phys. Rev. Research* **4**, 023002 (2022).